J. Indones. Math. Soc.
Vol. 32, No. 02 (2026), pp. 1–19.

Smoothed Particle Hydrodynamics for Heat Transfer in Plates: Analytical Validation and Geometric Effects of Internal Heat Sources

Riski Kurniawan[1*]

[1]Research Center for Computing, National Research and Innovation Agency (BRIN), Indonesia

Abstract. Accurate simulation of heat transfer is essential in many engineering applications. This study investigates heat transfer on thin plates by solving two-dimensional heat equations using the Smoothed Particle Hydrodynamics (SPH) method. The accuracy of the formulation is evaluated by comparing SPH results with analytical solutions for Dirichlet and Neumann boundary conditions, where small nRMSE values confirm good agreement. The method is then applied to plates with internal heat sources of different but equal-area geometries, showing that the star-shaped source yields the fastest heat transfer. These findings highlight the flexibility of SPH for modeling heat equations under complex geometries and boundary conditions.

Key words and Phrases: Heat transfer; smoothed particle hydrodynamics; Dirichlet boundary conditions; Neumann boundary conditions; internal heat source.

1. Introduction

Heat transfer is a fundamental physical process that plays a critical role in a wide range of engineering applications, from manufacturing and materials processing to energy systems and modern thermal technologies. These include heating plate panels, melting and freezing, metal casting, and thermal spraying [1, 2, 3, 4, 5]. Understanding the mechanisms of heat transfer is essential to improve energy efficiency, predict the thermal response of a system, and design devices that rely on temperature control.

Various experimental studies have been conducted to observe the conduction patterns and temperature distribution in solid materials [6, 7, 8]. However,

*Corresponding author : riski.kurniawan@brin.go.id

2020 Mathematics Subject Classification: 68U05, 65M25, 35Q70
Received: 23-09-2025, accepted: 25-01-2026.

experimental approaches are generally expensive and time-consuming. Therefore, mathematical models have become important alternatives for systematically studying heat transfer phenomena. In this study, the heat transfer process is modeled using the heat equation, which represents the most fundamental form of diffusion [9]. Conceptually, the heat equation belongs to the family of diffusion-type partial differential equations (PDEs), including the Extended Fisher–Kolmogorov equation (EFK) [10, 11] and the Kuramoto–Sivashinsky equation (KS) [12, 13], which are fourth-order equations.

The analytical solution of the heat equation depends heavily on the boundary conditions and becomes intractable when the geometry or boundaries are sufficiently complex. In such cases, numerical approaches provide a more practical framework for modeling realistic heat transfer scenarios [14, 15]. Classical grid-based schemes, such as the Finite Difference Method (FDM) [16], the Finite Volume Method (FVM) [17], and the Finite Element Method (FEM) [18], remain widely used for their robustness in structured domains. Various advanced discretization techniques have also been developed, including the One-Step One-Hybrid Block Method for nonlinear oscillatory PDEs [19], Hermite spline methods for the KS equation [20], and hybrid quintic Hermite spline collocation for the EFK equation [21]. Despite their strengths, grid-based methods can become restrictive when dealing with highly irregular boundaries, large deformations, or free-surface problems, motivating the use of more flexible mesh-free particle approaches such as Smoothed Particle Hydrodynamics (SPH).

SPH was first introduced by Lucy [22] and later developed independently by Gingold and Monaghan [23] for astrophysical simulations. Since then, it has been widely used to simulate solid mechanics and fluid dynamics [24, 25, 26]. Unlike grid-based schemes that require a predefined mesh, the SPH represents the domain as a set of interacting particles that carry quantities such as mass, position, velocity, and temperature. This mesh-free nature allows SPH to naturally handle large deformations, moving boundaries, and highly irregular geometries. The governing PDEs are reformulated as ordinary differential equations using integral approximations based on kernels, which form the core of the SPH methodology [27].

The use of SPH for heat transfer problems began with the pioneering work of Cleary and Monaghan [28], who demonstrated its ability to solve heat conduction equations. Since then, SPH has been extensively applied to a broad range of thermal processes, including conduction, convection, and radiation in complex geometries [29, 30, 31, 32, 33, 34, 35]. Recent developments have further expanded its applicability to enhanced heat transfer in nanofluids [36] and chemically reactive systems where thermal diffusion is coupled with reaction kinetics [37, 38]. Recent advances in manufacturing further emphasize the importance of modeling internal heat sources, as demonstrated by Lin et al. [39]), who applied a ray-tracing SPH model to represent laser-induced heating. In most classical heat transfer studies, the heat source is imposed directly within the heat equation [40, 41].

Although SPH has been applied in various heat transfer studies, several research gaps remain. The comprehensive validation of SPH against two-dimensional analytical solutions, especially for Dirichlet and Neumann boundary conditions, is still limited. In addition, the effect of the geometry of the internal heat source on the heat transfer rate in isolated plates, which is analytically challenging, has not been widely examined using SPH. To address these gaps, this study provides a systematic validation of the SPH against two-dimensional analytical solutions under Dirichlet and Neumann boundary conditions. Furthermore, we applied SPH to simulate heat transfer in plates containing internal heat sources of different geometries but equal area, allowing the assessment of how geometric variations influence heat transfer rates. The standard heat equation without a source term is employed, with the internal heat source imposed through Dirichlet conditions within the source region.

The remainder of this paper is organized as follows. Section 2 presents the mathematical formulation of the two-dimensional heat equation. Section 3 describes the SPH numerical scheme used to approximate the solution. Section 4 provides model validation by comparing the SPH results with analytical solutions. Section 5 investigates the influence of the geometry of the internal heat source on the heat transfer rate. Finally, Section 6 summarizes the main findings of this study.

2. Mathematical Model and Analytical Solutions

This section discusses the governing equations for heat transfer in a plate. Consider a thin plate $\Omega \subset \mathbb{R}^2$ made of heat-conducting material. Let $u(x, y, t)$ be the temperature of the plate at point $(x, y) \in \Omega$ and time t. This study is restricted to a rectangular plate $\Omega = [0, a] \times [0, b]$, where $a, b \in \mathbb{R}$.

Under the ideal assumption of uniform density and no external heat sources, u satisfies the two-dimensional heat equation:

$$\frac{\partial u}{\partial t} = \alpha \nabla^2 u = \alpha \left(\frac{\partial^2 u}{\partial x^2} + \frac{\partial^2 u}{\partial y^2} \right), \tag{1}$$

for $0 < x < a$, $0 < y < b$. Thermal diffusivity α is defined as

$$\alpha = \frac{\kappa}{\rho C_p}, \tag{2}$$

where κ is the thermal conductivity, C_p is the heat capacity, and ρ is the density of the material. In this study, the physical domain consists of a 10 cm $\times$ 10 cm carbon steel plate characterized by the material properties $\rho = 7854$ kg/m^3, $\kappa = 60.5$ W/(mK), and $C_p = 434$ J/(kgK). In steady state, equation (1) reduces to Laplace's equation.

The analytical solution of the two-dimensional heat equation (1) with generalized Dirichlet boundary conditions has been discussed by Hsu et al. [42]. As for Neumann boundary conditions, to the best of our knowledge, the analytical solutions have not been discussed in the literature. However, Subani et al. [43] have addressed this for the one-dimensional case, where the heat equation (1) in one-dimensional form with homogeneous Neumann boundary conditions is solved in two stages: variable separation and the superposition principle.

In the following, we present the analytical solution of the two-dimensional heat equation (1) with homogeneous Neumann boundary conditions. The plate temperature at the beginning of the observation is given as the initial condition:

$$u(x,y,0) = f(x,y), \quad (x,y) \in \Omega. \tag{3}$$

Furthermore, the homogeneous Neumann boundary conditions are as follows:

$$\begin{aligned} u_x(0,y,t) = u_x(a,y,t) = 0, &\quad 0 \le y \le b, t > 0, \\ u_y(x,0,t) = u_y(x,b,t) = 0, &\quad 0 \le x \le a, t > 0. \end{aligned} \tag{4}$$

Physically, this means isolating the four sides of the plate so that no heat enters or leaves the plate through these sides.

Using a procedure similar to [43], we obtain an analytical solution of the heat equation (1) with the initial conditions (3) and the boundary conditions (4) as follows:

$$\begin{aligned} u(x,y,t) = A_{00} &+ \sum_{m=1}^{\infty} A_{m0} \cos\left(\frac{m\pi}{a}x\right) e^{-\alpha\pi^2\left(\frac{m}{a}\right)^2 t} + \sum_{n=1}^{\infty} A_{0n} \cos\left(\frac{n\pi}{b}y\right) e^{-\alpha\pi^2\left(\frac{n}{b}\right)^2 t} \\ &+ \sum_{m=1}^{\infty}\sum_{n=1}^{\infty} A_{mn} \cos\left(\frac{m\pi}{a}x\right) \cos\left(\frac{n\pi}{b}y\right) e^{-\alpha\pi^2\left(\left(\frac{m}{a}\right)+\left(\frac{n}{b}\right)\right)^2 t}, \end{aligned} \tag{5}$$

where

$$\begin{aligned} A_{00} &= \int_0^a \int_0^b f(x,y)\, dy\, dx, & A_{m0} &= \int_0^a \int_0^b f(x,y) \cos\left(\frac{m\pi}{a}x\right)\, dy\, dx, \\ A_{0n} &= \int_0^a \int_0^b f(x,y) \cos\left(\frac{n\pi}{b}y\right)\, dy\, dx, & A_{mn} &= \int_0^a \int_0^b f(x,y) \cos\left(\frac{m\pi}{a}x\right) \cos\left(\frac{n\pi}{b}y\right)\, dy\, dx. \end{aligned}$$

The detailed derivation of this analytical solution is provided in the Appendix.

3. Numerical Method

In this section, we describe the SPH formulation used to approximate the two-dimensional heat equation (1). The domain Ω is discretized into a number of N particles with the initial positions of the i-particles being $\mathbf{x}_i = (x_i, y_i)$, $i = 1, 2, \ldots, N$. Two types of initial particle arrangement are commonly used: structured and unstructured, as illustrated in Fig. 1. A structured layout produces higher operator accuracy [44], but is less flexible to capture intricate geometries. In contrast, an unstructured distribution allows particles to reach narrow features of the domain, although the resulting particle disorder may introduce extra numerical noise [45].

The function u at $\mathbf{x}_i$ and time t can be approximated by volume integration using the kernel function (also called the weight function) W, as follows

$$u(\mathbf{x}_i, t) \approx [u(\mathbf{x}_i, t)] \equiv \int_\Omega u(\mathbf{x}_j, t) W(r_{ij}, h)\, d\mathbf{x}_j, \tag{6}$$

for $j = 1, 2, \ldots, N$, where r_{ij} is the distance between the particles i and j, and h are the smoothing lengths. Consistent with typical SPH settings [24, 27, 45], we

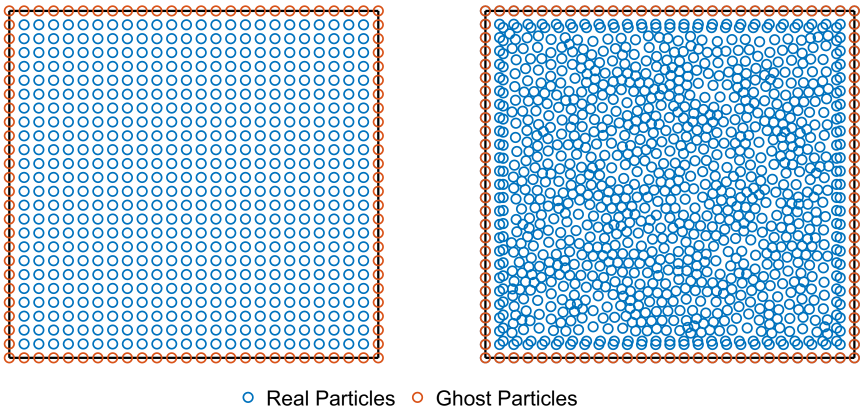

FIGURE 1. Particle arrangements used in SPH: (left) structured distribution, (right) unstructured distribution.

define the smoothing length as $h = 1.2\Delta p$, where Δp is the initial spacing of the particles.

Neighborhood particles are a crucial component in particle kernel approximation. Define the vector $\mathbf{r_{ij}}$ as the distance vector between particles i and j,

$$\mathbf{r_{ij}} = \begin{pmatrix} x_i - x_j \\ y_i - y_j \end{pmatrix}.$$

The distance between the target particle i and the neighboring particle j is defined using the Euclidean norm

$$r_{ij} = \|\mathbf{r_{ij}}\|_2 = \sqrt{(x_i - x_j)^2 + (y_i - y_j)^2}.$$

In this study, we use a multiplier $k = 2$ on the smoothing length. If $r_{ij} \leq 2h$, then the particle j is considered a neighbor of the particle i. For example, Fig. 2 (left) illustrates the definition of neighboring particles, where particle i has 20 neighboring particles.

Furthermore, several smoothing kernels are commonly used, including cubic spline (B-spline), Gaussian, Supergaussian, Quadratic, and Quintic kernels. The kernel function used in this study is the cubic spline, which is given as

$$W(s) = \sigma \begin{cases} 1 - \frac{3}{2}s^2 + \frac{3}{4}s^3, & 0 \leq s \leq 1 \\ \frac{1}{4}(2-s)^3, & 1 < s \leq 2 \end{cases}, \tag{7}$$

where $s = \frac{r_{ij}}{h}$. The constant σ varies for each dimension to satisfy the kernel normalization requirements. For a two-dimensional system, $\sigma = \frac{10}{7\pi h^2}$. Note that the kernel (7) is a smooth polynomial function, which allows it to be differentiated at all s. The cubic spline kernel function and its derivatives are plotted in Fig. 2 (right). It is also important to note that the values of the kernel function and its

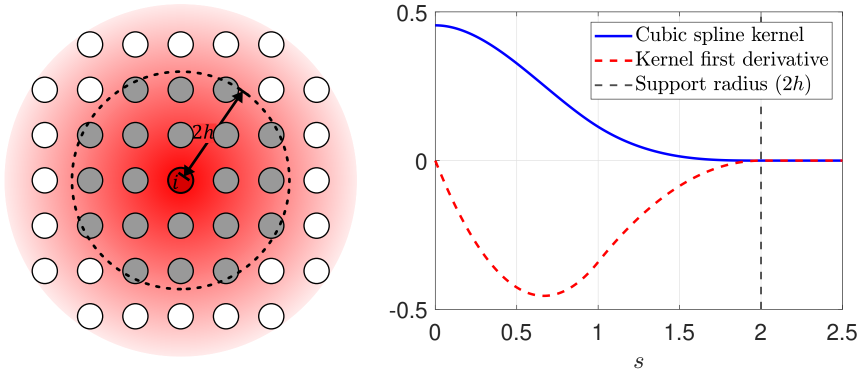

FIGURE 2. (Left) Particle Neighborhood. (Right) Kernel function.

derivatives are zero for $s > 2$, meaning that particles located more than $2h$ away from the target particle do not contribute to the approximation.

Since the domain is modeled as discrete particles, the continuous integral (6) needs to be converted to a discrete sum over all particles in the domain. Let $\mathbb{S}_i$ be the set of neighboring particles j surrounding the target particle i, which is discretized as

$$\mathbb{S}_i \equiv \{j = 1, 2, ..., N | j \neq i\}. \tag{8}$$

The approximation (6) can be expressed in its discrete particle form as follows:

$$u(\mathbf{x}_i, t) \approx \langle \phi(\mathbf{x}_i, t) \rangle \equiv \sum_{j \in \mathbb{S}_i} \frac{m_j}{\rho_j} u(\mathbf{x}_j, t) W(r_{ij}, h), \tag{9}$$

where m_j and ρ_j are the mass and density of the particle j, respectively.

The kernel function derivative is used for the Laplace approximation. The kernel gradient vector is given as

$$\nabla W(r_{ij}, h) = \begin{pmatrix} dW_x \\ dW_y \end{pmatrix}, \tag{10}$$

where

$$dW_x = \frac{x_{ij}(\partial W/\partial s)}{r_{ij} h}, \quad dW_y = \frac{y_{ij}(\partial W/\partial s)}{r_{ij} h}.$$

Finally, the gradient and Laplace approximations of the SPH method are given as follows:

$$\nabla u(\mathbf{x}_i, t) \approx \langle \nabla u_i \rangle = \sum_{j \in \mathbb{S}_i} \frac{m_j}{\rho_j} (u_j - u_i) \nabla W_{ij}, \tag{11}$$

$$\nabla^2 u(\mathbf{x}_i, t) \approx \langle \nabla^2 u_i \rangle = 2 \sum_{j \in \mathbb{S}_i} \frac{m_j}{\rho_j} \frac{u_j - u_i}{r_{ij}^2} \left(\mathbf{r}_{ij} \cdot \nabla W_{ij} \right). \tag{12}$$

After approximating the Laplace form using the SPH method, we proceed with the time integration of the heat equation (1). To ensure a stable solution, the time step Δt must satisfy the Courant-Friedrichs-Lewy (CFL) condition. This condition ensures that the numerical domain of dependence contains the physical domain of dependence, which means that the numerical propagation speed must not be smaller than the physical propagation speed [46, 47]. In the case of two-dimensional heat diffusion, the time step Δt is formulated as

$$\Delta t \leq \frac{h^2}{4\alpha}, \tag{13}$$

The temperature of the particle i at time t^{n+1} is then computed using the forward Euler method, given by

$$u_i{}^{n+1} = u_i{}^{n} + \Delta t \nabla^2 u_i^n. \tag{14}$$

To handle the boundary value problem, SPH utilizes the concept of ghost particles, which are additional particles located outside the domain or around the $\partial\Omega$ boundary; refer back to Fig. 1. These particles are not included in the SPH computation, but are arranged to approximate the prescribed boundary conditions. Dirichlet boundary conditions are enforced by setting the temperature of the ghost particles equal to the specified boundary values, as described in [32]. Implementing homogeneous Neumann boundary conditions poses additional challenges, such as assigning the temperatures of ghost particles so that the normal temperature gradient vanishes, which requires arranging the particles near the boundary in a structured manner so that the ghost particle temperature can be mirrored from the interior particle across the boundary.

In summary, the steps for using the SPH method to simulate heat transfer are outlined in Algorithm 1.

Algorithm 1 SPH method for solving heat equations (1)

```
Require: Ω = {(x, y)} ⊂ R^2, u(x, y, 0), t_final
Ensure: u(x, y, t)
Discretize Ω into N particles
Discretize [0, t_final] into {t^n : n = 1, ..., N_t}
Form an adjacency matrix that defines the neighboring particles of each particle.
for n = 1, ..., N_t do
    Calculate ∇^2 u using (12)
    Calculate u^{n+1} using (14)
    Set the ghost particle value
end for
```

All simulations were performed on a computer equipped with an AMD Ryzen 9 PRO 5945 processor (12 cores, 24 CPUs, 3.0 GHz), 128 GB RAM, and a Windows 11 operating system. Numerical calculations were performed using MATLAB R2024b.

4. Model Validation

In this section, the SPH results obtained using the numerical procedure described in Algorithm 1 are compared with the corresponding analytical solutions to assess the accuracy of the method. The computational domain is expressed as $\Omega = [0,1]$ dm $\times$ $[0,1]$ dm. The plate is discretized using a structured particle arrangement, where Δx and Δy denote the initial particle spacing in the x- and y-directions, respectively, and are taken to be equal in this study.

The agreement between the SPH and the analytical reference is quantified using the normalized root mean square error (nRMSE). This metric is chosen because it provides a scale-independent measure of accuracy, allowing the error to be interpreted relative to the thermal range of the system and enabling fair comparison between different test cases. The nRMSE is defined as

$$\text{nRMSE} = \frac{\text{RMSE}}{\hat{u}_{\max} - \hat{u}_{\min}}, \quad \text{RMSE} = \sqrt{\frac{\sum_{i=1}^{N}(u_i - \hat{u}_i)^2}{N}}, \tag{15}$$

where $\hat{u}_{\max}$ and $\hat{u}_{\min}$ denote the maximum and minimum values of the analytical solution in the domain, respectively.

4.1. **Steady-state heat conduction.**

In the first validation test, the steady-state heat conduction problem is examined. The boundary conditions follow those used in the reference study [48], which are defined as

$$\begin{aligned} u(x,1,t) &= \frac{400}{\pi}\sin(\pi x)^\circ\text{C}, \\ u(x,0,t) &= u(0,y,t) = u(1,y,t) = 0^\circ\text{C}. \end{aligned} \tag{16}$$

The analytical solution of Laplace's equation associated with this configuration is given as follows

$$u(x,y) = \frac{400}{\pi \sinh \pi}\sinh(\pi y)\sin(\pi x)^\circ\text{C}. \tag{17}$$

The reference study [48] solves the Laplace equation numerically using FEM and FDM. In contrast, the present work employs the full transient heat equation and advances the solution over time until it converges to the steady state. The initial condition is specified as a uniform temperature distribution:

$$u(x,y,0) = 0^\circ\text{C}, \quad (x,y) \in \Omega. \tag{18}$$

The SPH simulation is performed using several particle spacings, namely $\Delta x =$ 0.1 dm, 0.02 dm, and 0.01 dm. For each resolution, the particles are uniformly distributed within the computational domain $[0,1]\times[0,1]$ dm, resulting in $N = 2601$ particles for $\Delta x = 0.02$ dm. The solution is advanced in time to $t = 600$ s using a time step of $\Delta t = 0.02$ s. During the computation, the boundary conditions (16) are imposed directly on the gost particles.

The evolution of the temperature distribution for the representative resolution $\Delta x = 0.02$ dm is illustrated in Fig. 3. The heat gradually diffuses downward from the upper edge. By $t = 600$ s, the solution does not exhibit significant temporal changes, indicating that the steady state has been effectively reached.

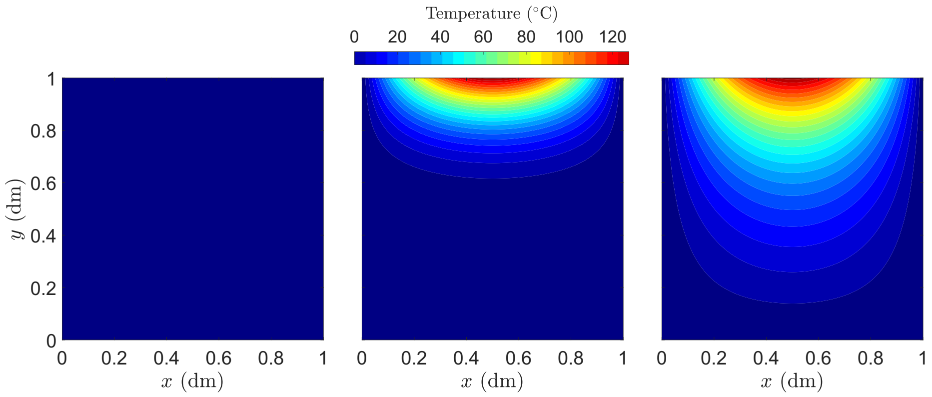

FIGURE 3. Temperature distribution for steady-state heat conduction test at $t = 0$ s (left), $t = 10$ s (middle), and $t = 600$ s (right).

To quantify the accuracy of the SPH method, we calculate the RMSE between the steady-state temperature and the analytical solution. The RMSE values for different particle spacings Δx are reported in Table 1. The error decreases consistently with mesh refinement, indicating good numerical convergence. Compared with the reference numerical schemes, SPH achieves a higher precision than the FDM results of [48], while the FEM solution in [48] remains the most accurate among the three methods. The table also lists the computational time required for each resolution, showing the expected increase in running time as the number of particles grows. Although accuracy improves at finer resolutions, the computational cost increases accordingly.

TABLE 1. RMSE values of numerical results for different spatial resolutions, along with the corresponding number of particles and computational time of SPH.

Δx (dm)	N	Comp. time (s)	RMSE		
			SPH	FEM[48]	FDM[48]
0.10	121	14	0.403	0.367	1.749
0.02	2601	432	0.112	0.015	0.353
0.01	10201	1783	0.059	-	-

4.2. **Nonhomogeneous Dirichlet boundary condition.** For this case, consider a plate with an initial temperature distribution given by

$$u(x, y, 0) = \sin(\pi x) + \sin(\pi y). \tag{19}$$

The four sides of the plate are subjected to sinusoidal boundary conditions that vary spatially and decay exponentially over time, given as

$$\begin{aligned} u(0, y, t) = u(1, y, t) = \sin(\pi y) e^{-\pi^2 \alpha t}, \\ u(x, 0, t) = u(x, 1, t) = \sin(\pi x) e^{-\pi^2 \alpha t}. \end{aligned} \tag{20}$$

In this simulation, a particle spacing of $\Delta x = 0.02$ dm is used, resulting in a total of $N = 2601$ particles. The simulation is performed up to $t = 20$ s with a time step of $\Delta t = 0.02$ s, and the total computational time is approximately 14 s. The time evolution of the temperature field is shown in Fig. 4, where the initial sinusoidal pattern gradually decays under exponentially decreasing boundary forcing. As time increases, the temperature amplitude decreases, and the contours progressively flatten toward a more uniform radial distribution.

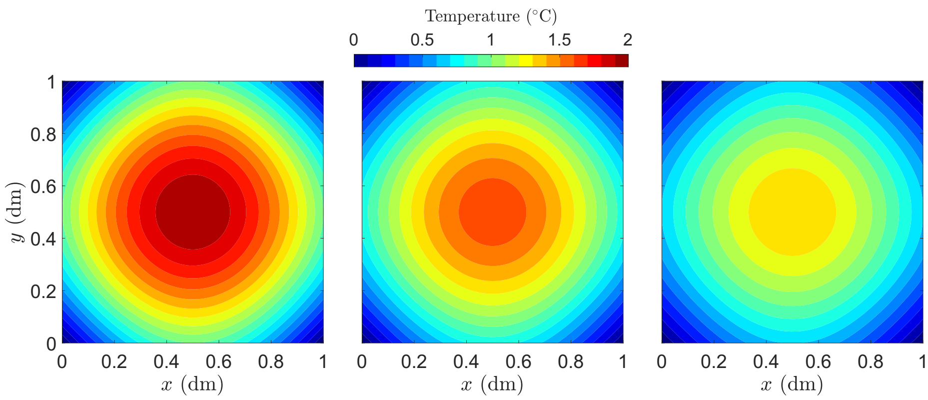

FIGURE 4. Temperature distribution for nonhomogeneous Dirichlet test at $t = 0$ s (left), $t = 10$ s (middle), and $t = 20$ s (right).

The heat equation (1) with the initial condition (19) and the boundary condition (20), has been studied by Hsu et al. [42]. The analytical solution is given as

$$u(x, y, t) = (\sin(\pi x) + \sin(\pi y))\, e^{-\alpha \pi^2 t}. \tag{21}$$

A comparison of the contours between the analytical and SPH solutions at $t = 10$ s is shown in Fig. 5 (left). It can be observed that, near the center of the plate, the SPH results are slightly ahead of the analytical solution. However, the SPH contour fits perfectly with the analytical solution. During computation, the nRMSE is evaluated using equations (15), and the results are shown in Fig. 5 (right). Although the nRMSE increases with the simulation time, it remains very small, staying below 6×10^{-3}. This shows that SPH performs excellently in approximating the analytical solution.

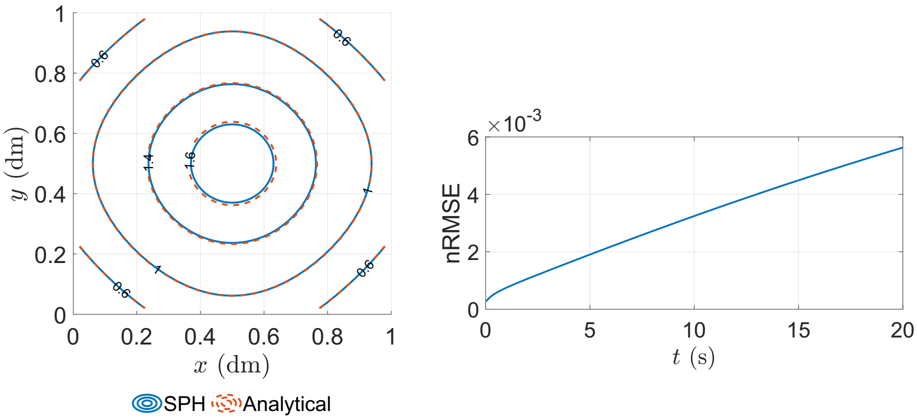

FIGURE 5. Error analysis for nonhomogeneous Dirichlet test. (Left) temperature contours at $t = 10$ s, (right) nRMSE of SPH over time.

4.3. **Homogeneous Neumann boundary condition.** The final test case aims to evaluate the performance of SPH in simulating heat transfer when the domain boundaries are isolated. In this case, all four sides of the plate are subjected to homogeneous Neumann boundary conditions, as specified in equations (4). The initial heat distribution of the plate is given by

$$u(x, y, 0) = x - y. \tag{22}$$

From equation (5), we derive the analytical solution of the heat equation (1) with the boundary conditions (4) and the initial conditions (22), given by the following expression:

$$u(x, y, t) = \frac{2}{\pi^2}\left[\sum_{m=1}^{\infty} \frac{(-1)^m - 1}{m^2} \cos(m\pi x) e^{-\alpha(m\pi)^2 t} + \sum_{n=1}^{\infty} \frac{1-(-1)^n}{n^2} \cos(n\pi y) e^{-\alpha(n\pi)^2 t}\right] \tag{23}$$

The computational domain is discretized using a space of $\Delta x = 0.02$ dm. To properly enforce the boundary conditions (4), the ghost particles are positioned just outside the domain. Consequently, the particles are arranged from $-\frac{\Delta x}{2}$ to $1 + \frac{\Delta x}{2}$ in both spatial directions, resulting in a total of $N = 2704$ particles. The simulation is carried out up to $t = 20$ s and requires approximately 20 s computational time.

The temporal evolution of the temperature field is shown in Fig. 6. Under homogeneous Neumann boundary conditions, the heat within the plate is gradually redistributed, whereas no flux crosses the boundaries. As diffusion progresses, spatial temperature variations diminish and the solution approaches a uniform state corresponding to the average of the initial condition.

The SPH solution at $t = 10$ s is shown as a contour in Fig. 7 (left), along with the analytical solution given by (23). It can be observed that the SPH solution contour closely matches the analytical solution contour. The nRMSE value during

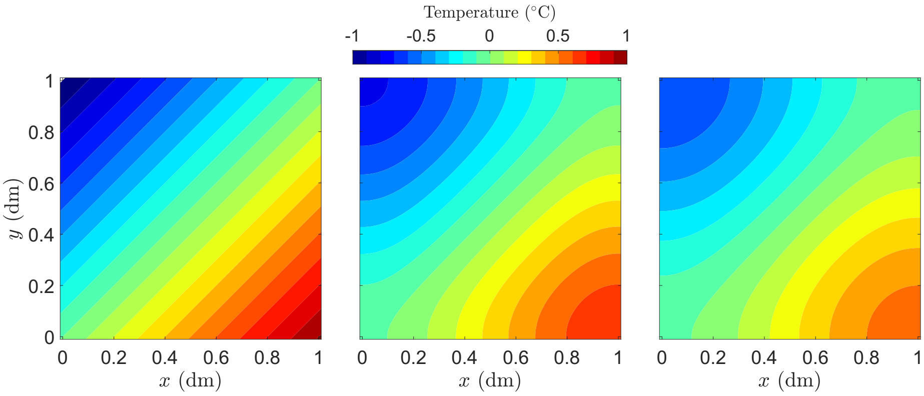

FIGURE 6. Temperature distribution for homogeneous Neumann test at $t = 0$ s (left), $t = 10$ s (middle), and $t = 20$ s (right).

the simulation time is shown in Fig. 7 (right). From the beginning of the simulation, nRMSE decreases but increases after $t = 1$ s. However, the nRMSE value is still very small, that is, below 1.2×10^{-3}. This very small error shows that the SPH is very good at approaching the analytical solution.

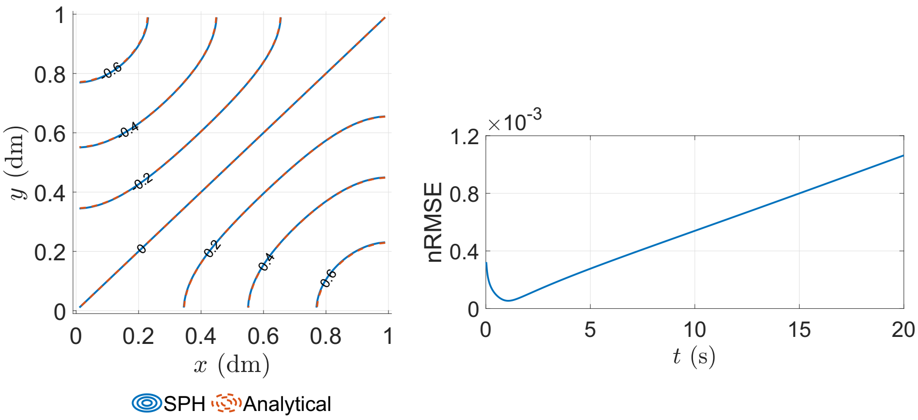

FIGURE 7. Error analysis for homogeneous Neumann test. (Left) temperature contours at $t = 10$ s, (right) nRMSE of SPH over time.

5. Influence of Heat Source Geometry

Finally, SPH is used to simulate heat transfer in more complex cases. We investigate the effect of an internal heat source located in the center of the plate on the rate of heat spreading. Heat sources with various geometries, all having the same area, are considered. The objective is to analyze which geometric shapes distribute heat more rapidly than others. All four sides of the plate are insulated, which prevents heat from entering or exiting the edges. This case is quite complex to solve analytically, as it involves nonhomogeneous Dirichlet and homogeneous Neumann boundary conditions, and the geometric shape of the heat source is not simple. To the best of our knowledge, this issue has not been previously discussed in the literature.

We tested six heat source geometries: circular, triangular, square, hexagonal, star, and star of David. The radius of the circular heat source is 1 cm, and all heat sources have the same area. The dimensions of these heat sources are shown in Fig. 8. Initially, the plate has a uniform temperature of 300°K. Then a constant heat source of 370°K is applied.

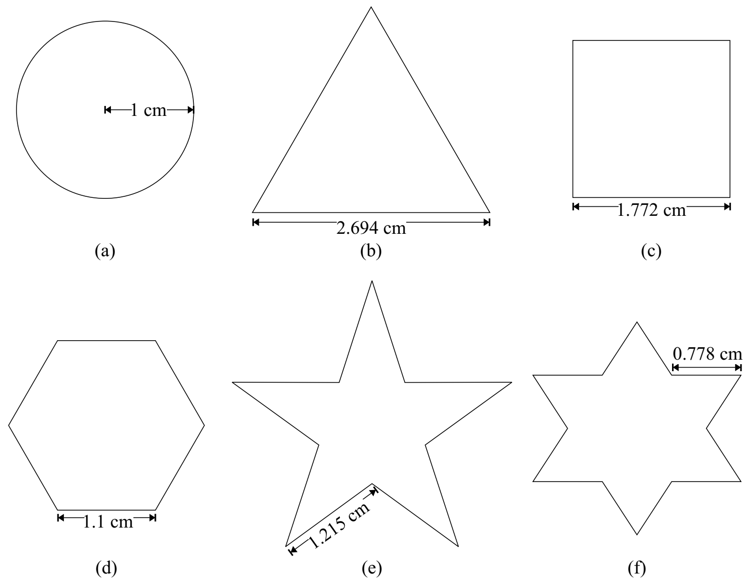

FIGURE 8. Dimensions of heat source geometry, (a) circular, (b) triangular, (c) square, (d) hexagonal, (e) star, (f) star of David.

To allow particles to reach narrow corners, we use an unstructured particle distribution, and the particle spacing Δp is set to be no larger than 0.2 cm. The simulation is carried out up to $t = 30$ s using a time step of $\Delta t = 0.2$ s. The number of particles and the corresponding computational time for each heat-source geometry are summarized in Table 2.

The heat distribution at $t = 30$ s for all heat sources is shown in Fig. 9. It can be seen that the heat spreads radially toward the edges of the plate, forming a circular pattern. The temperature decreases monotonically from the center to the edges. It can be observed that, among all heat sources, those with star geometries disperse heat more rapidly.

TABLE 2. Number of particles and computational time for each heat source geometry.

Geometry	Circular	Triangular	Square	Hexagonal	Star	Star of David
N	4259	4268	4308	4227	4259	4230
Comp. time (s)	37	36	39	37	37	35

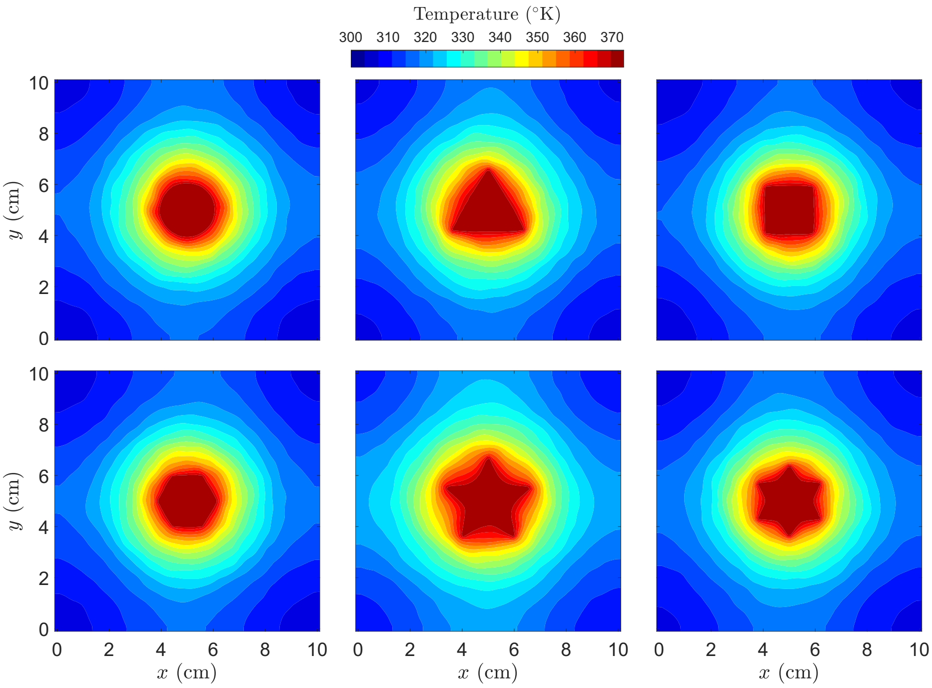

FIGURE 9. Heat distribution at $t = 30$ s, (a) circular, (b) triangular, (c) square, (d) hexagonal, (e) star, (f) star of David.

To compare the rate of heat propagation, we plot the contours of a selected temperature for all heat source geometries. Here, we plot the contour for $u = 330°\mathrm{K}$, which is depicted in Fig. 10 (left). It can be seen that the temperature range $u = 330°\mathrm{K}$ for star geometries is wider than for other geometries. In addition, we also calculated the average plate temperature outside the heat source $\bar{u}$, which is shown in Fig. 10 (right). The average temperature also shows that the star geometry disperses heat more quickly, compared to the other five geometries. The star geometry spreads heat faster because its extended tips reach farther toward cooler areas of the plate, creating stronger temperature differences that accelerate diffusion.

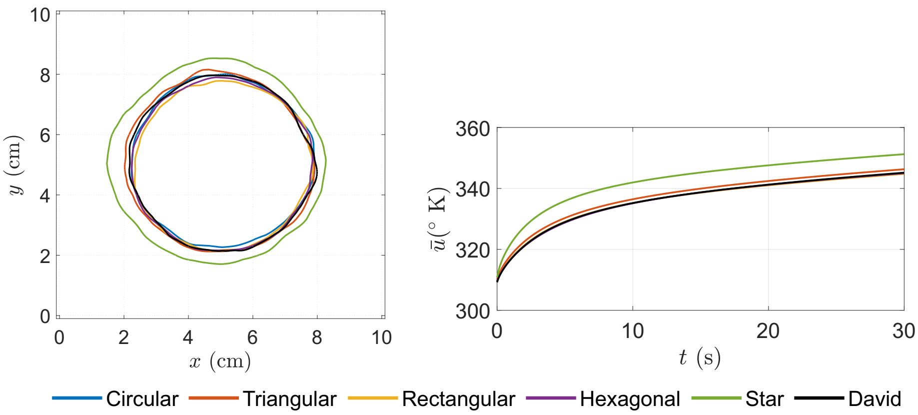

FIGURE 10. (Left) contours of $u = 330°$ K at $t = 30$ s. (Right) average temperature as a function of time.

6. Conclusion

This study demonstrates that the Smoothed Particle Hydrodynamics (SPH) method can accurately simulate two-dimensional heat transfer on thin plates under various boundary conditions. Validation against analytical solutions for Dirichlet and homogeneous Neumann problems shows excellent agreement, as indicated by consistently low nRMSE values. The method was also applied to plates containing internal heat sources of equal area but different geometries, revealing that star-shaped sources promote faster heat spread than other configurations. These results highlight the flexibility of SPH in handling complex boundary specifications and geometric variations.

Despite these strengths, the present formulation has several limitations. SPH requires user-defined parameters such as the smoothing length and the kernel function, both of which introduce uncertainty. In addition, the model used here solves only a scalar temperature field with fixed particle positions, which does not exploit the full potential of SPH for deforming or moving domains. The governing physics is limited to pure conduction, and the validation is restricted to rectangular domains and analytical benchmarks. Future work may include validation against analytical solutions in circular domains as well as comparisons with laboratory experiments, which will require more complex governing equations that incorporate heat sources, convection, or phase change. Extensions to fully coupled thermo-fluid systems, moving particles, and three-dimensional geometries would further strengthen SPH as a versatile tool for realistic heat-transfer modeling.

Acknowledgement. The author thanks the editors and reviewers who took the time to review the article.

Appendix

Details of the search for analytical solutions of the two-dimensional heat equation for homogeneous Neumann boundary conditions:

1. Separation of Variables
Suppose u can be expressed as the product of three functions, namely:

$$u(x, y, t) = X(x)Y(y)T(t) \tag{24}$$

By substituting (24) into the model (1) and applying the boundary conditions (4), we obtain the Sturm-Liouville problem

$$X'' + BX = 0, \quad X_x(0) = X_x(a) = 0, \tag{25}$$

$$Y'' + CY = 0, \quad Y_y(0) = Y_y(b) = 0, \tag{26}$$

and

$$T' - \alpha(-B - C)T = 0. \tag{27}$$

The solutions of (25) and (26) are

$$X_m(x) = B_m \cos(\omega_m x), \tag{28}$$

$$Y_n(y) = C_n \cos(\omega_n y), \tag{29}$$

where $\omega_m = \frac{m\pi}{a}$ and $\omega_n = \frac{n\pi}{b}$. Meanwhile, the solution (27) is

$$T_{mn}(t) = e^{-\lambda_{mn}^2 t},$$

where

$$\lambda_{mn}^2 = \alpha(\omega_m^2 + \omega_n^2), \quad \text{for } m, n \in \mathbb{N}$$

2. Superposition
For each pair m, n we have

$$\begin{aligned} u_{mn}(x, y, t) &= X_m(x)Y_n(y)T_{mn}(t) \\ &= A_{mn} \cos(\omega_m x) \cos(\omega_n y) e^{-\lambda_{mn}^2 t}, \end{aligned}$$

as a solution, where $A_{mn} = B_m C_n$. For each selection of constants A_{mn}, using the superposition principle, we obtain a general solution to the heat equation (1) with boundary conditions (4) as

$$u(x, y, t) = \sum_{m=0}^{\infty} \sum_{n=0}^{\infty} A_{mn} \cos(\omega_m x) \cos(\omega_n y) e^{-\alpha(\omega_m^2 + \omega_n^2)t}. \tag{30}$$

From the initial condition (19) we have

$$f(x, y) = \sum_{m=0}^{\infty} \sum_{n=0}^{\infty} A_{mn} \cos(\omega_m x) \cos(\omega_n y) \tag{31}$$

which is a double Fourier series for $f(x, y)$. If f is a function C^2, then

$$A_{mn} = \frac{4}{ab} \int_0^a \int_0^b f(x, y) \cos(\omega_m x) \cos(\omega_n y) dy dx \tag{32}$$

REFERENCES

[1] N. Perakis, O. J. Haidn, and M. Ihme, "Heat transfer augmentation by recombination reactions in turbulent reacting boundary layers at elevated pressures," *International Journal of Heat and Mass Transfer*, vol. 178, no. 121628, 2021. `https://doi.org/10.1016/j.ijheatmasstransfer.2021.121628`.

[2] M. A. S. M. Hassan, Z. M. Razlan, S. A. Bakar, A. A. Rahman, M. A. Rojan, W. K. Wan, Z. Ibrahim, A. A. Ishak, and M. J. M. Ridzuan, "Derivation and validation of heat transfer model for spark-ignition engine cylinder head," *Appl. Therm. Eng.*, vol. 225, no. 120240, 2023. `https://doi.org/10.1016/j.applthermaleng.2023.120240`.

[3] H. Budhia and F. Kreith, "Heat transfer with melting or freezing in a wedge," *International Journal of Heat and Mass Transfer*, vol. 16, no. 1, pp. 195–211, 1973. `https://doi.org/10.1016/0017-9310(73)90262-7`.

[4] P. W. Cleary, J. Ha, M. Prakash, and T. Nguyen, "3d sph flow predictions and validation for high pressure die casting of automotive components," *Applied Mathematical Modelling*, vol. 30, no. 11, pp. 1406–1427, 2006. `https://doi.org/10.1016/j.apm.2006.03.012`.

[5] B. Gnanasekaran, G. R. Liu, Y. Fu, G. Wang, W. Niu, and T. Lin, "A smoothed particle hydrodynamics (sph) procedure for simulating cold spray process-a study using particles," *Surface and Coatings Technology*, vol. 377, no. 124812, 2019. `https://doi.org/10.1016/j.surfcoat.2019.07.036`.

[6] F. A. W. Hamad, "Experimental study of natural convection heat transfer in inclined cylindrical annulus," *Solar & Wind Technology*, vol. 6, no. 5, pp. 573–579, 1989. `https://doi.org/10.1016/0741-983X(89)90093-3`.

[7] S. O. Atayılmaz and I. Teke, "Experimental and numerical study of the natural convection from a heated horizontal cylinder wrapped with a layer of textile material," *Int. Comm. in Heat and Mass Transfer*, vol. 37, no. 1, pp. 58–67, 2010. `https://doi.org/10.1016/j.icheatmasstransfer.2009.09.009`.

[8] A. Valizadeh and J. J. Monaghan, "A study of solid wall models for weakly compressible sph," *J Comput Phys.*, vol. 300, pp. 5–19, 2015. `https://doi.org/10.1016/j.jcp.2015.07.033`.

[9] W. A. Strauss, *Partial Differential Equations: An Introduction.* New Jersey: John Wiley & Sons, 2008.

[10] L. A. Peletier and W. C. Troy, "Spatial patterns described by the extended fisher–kolmogorov equation: Periodic solutions," *SIAM J. Math. Anal.*, vol. 28, no. 6, pp. 1317—-1353, 1997. `https://doi.org/10.1137/S0036141095280955`.

[11] V. Rottschäfer and C. E. Wayne, "Existence and stability of traveling fronts in the extended fisher–kolmogorov equation," *J. Differential Equations*, vol. 176, no. 2, pp. 532—560, 2001. `https://doi.org/10.1006/jdeq.2000.3984`.

[12] Y. Kuramoto, "Diffusion-induced chaos in reaction systems," *Progr. Theoret. Phys. Suppl.*, vol. 64, pp. 346—367, 1978. `https://doi.org/10.1143/PTPS.64.346`.

[13] G. I. Sivashinsky, "On flame propagation under conditions of stoichiometry," *SIAM J. Appl. Math.*, vol. 39, no. 1, pp. 67—82, 1980. `https://doi.org/10.1137/0139007`.

[14] R. Liu, W. Zhang, S. Han, H. Du, P. Cui, Z. Ma, X. Feng, and W. Zhang, "A numerical heat transfer model and performance evaluation of coaxial geothermal heat exchanger under soil freezing conditions," *Applied Thermal Engineering*, vol. 266, no. 125538, 2025. `https://doi.org/10.1016/j.applthermaleng.2025.125538`.

[15] D. Jiang, J. Deng, D. Zhang, X. Zhou, C. Xiao, W. Tian, J. Zhang, and G. H. Su, "Evaluation of a numerical model for predicting flow and heat transfer in a hexagonal helical cruciform seven-rods bundle and analysis of rod bundle size independence," *International Communications in Heat and Mass Transfer*, vol. 161, no. 108409, 2025. `https://doi.org/10.1016/j.icheatmasstransfer.2024.108409`.

[16] Y. Hong, J. Lin, A. H. D. Cheng, and Y. Wang, "Simulation of heat transfer in poiseuille pipe flow via generalized finite difference method with a space stepping algorithm," *Computers & Mathematics with Applications*, vol. 163, pp. 136–145, 2024. `https://doi.org/10.1016/j.camwa.2024.03.023`.

[17] E. M. Filho, L. O. Seman, and V. d. P. Nicolau, "Simulation of a cubesat with internal heat transfer using finite volume method," *Applied Thermal Engineering*, vol. 193, no. 117039, 2021. https://doi.org/10.1016/j.applthermaleng.2021.117039.

[18] M. Fayz-Al-Asad, F. Mebarek-Oudina, H. Vaidya, M. S. Hasan, M. M. A. Sarker, and A. I. Ismail, "Finite element analysis for magneto-convection heat transfer performance in vertical wavy surface enclosure: Fin size impact," *Frontiers in Heat and Mass Transfer*, vol. 22, no. 3, pp. 817–837, 2024. https://doi.org/10.32604/fhmt.2024.050814.

[19] M. Farhan, Z. Omar, F. Mebarek-Oudina, J. Raza, R. V. Shah, Z. Choudari, and O. D. Makinde, "Implementation of the one-step one-hybrid block method on the nonlinear equation of a circular sector oscillator," *Comput Math Model*, vol. 31, pp. 116–132, 2020. https://doi.org/10.1007/s10598-020-09480-0.

[20] Priyanka., S. Arora, F. Mebarek-Oudina, and S. Sahani, "Super convergence analysis of fully discrete hermite splines to simulate wave behaviour of kuramoto–sivashinsky equation," *Wave Motion*, vol. 121, no. 103187, 2023. https://doi.org/10.1016/j.wavemoti.2023.103187.

[21] Priyanka., F. Mebarek-Oudina, S. Sahani, and S. Arora, "Travelling wave solution of fourth order reaction diffusion equation using hybrid quintic hermite splines collocation technique," *Arab. J. Math.*, vol. 13, pp. 341–367, 2024. https://doi.org/10.1007/s40065-024-00459-y.

[22] L. B. Lucy, "A numerical approach to the testing of the fission hypothesis," *The Astronomical Journal*, vol. 82, pp. 1013–1024, 1977. https://doi.org/10.1086/112164.

[23] R. A. Gingold and J. J. Monaghan, "Smoothed particle hydrodynamics: theory and application to non-spherical stars," *Mon. Not. R. Astron. Soc*, vol. 181(3), pp. 375–389, 1977. https://doi.org/10.1093/mnras/181.3.375.

[24] J. J. Monaghan, "Simulating free surface flows with sph," *Journal of Computational Physics*, vol. 110(2), pp. 399–406, 1994. https://doi.org/10.1006/jcph.1994.1034.

[25] L. Han and X. Hu, "Sph modeling of fluid-structure interaction," *Journal of Hydrodynamics*, vol. 30, pp. 62–69, 2018. https://doi.org/10.1007/s42241-018-0006-9.

[26] A. Colagrossi and M. Landrini, "Numerical simulation of interfacial flows by smoothed particle hydrodynamics," *Journal of Computational Physics*, vol. 191, no. 2, pp. 448–475, 2003. https://doi.org/10.1016/S0021-9991(03)00324-3.

[27] G. R. Liu and M. B. Liu, *Smoothed Particle Hydrodynamics: a Meshfree Particle Method*. New Jersey: World Scientific, 2003. https://doi.org/10.1142/5340.

[28] P. W. Clearly and J. J. Monaghan, "Conduction modelling using smoothed particle hydrdynamics," *Journal of Computational Physics*, vol. 148, no. 1, pp. 227–264, 1999. https://doi.org/10.1006/jcph.1998.6118.

[29] A. Farrokhpanah, M. Bussmann, and J. Mostaghimi, "New smoothed particle hydrodynamics (sph) formulation for modeling heat conduction with solidification and melting," *Numerical Heat Transfer, Part B: Fundamentals*, vol. 71, no. 4, pp. 299–312, 2017. https://doi.org/10.1080/10407790.2017.1293972.

[30] X. Dong, G. Hao, and R. Yu, "Two-dimensional smoothed particle hydrodynamics (sph) simulation of multiphase melting flows and associated interface behavior," *Engineering Applications of Computational Fluid Mechanics*, vol. 16, no. 1, pp. 588–629, 2022. https://doi.org/10.1080/19942060.2022.2026820.

[31] S. Yu, X. Ren, and J. Zhang, "Using an improved sph algorithm to simulate thermo-hydro-mechanical-damage coupling problems in rock masses," *Case Studies in Thermal Engineering*, vol. 47, no. 103085, 2023. https://doi.org/10.1016/j.csite.2023.103085.

[32] K. C. Ng, Y. L. Ng, T. W. H. Sheu, and A. Alexiadis, "Assessment of smoothed particle hydrodynamics (sph) models for predicting wall heat transfer rate at complex boundary," *Engineering Analysis with Boundary Elements*, vol. 111, pp. 195–205, 2020. https://doi.org/10.1016/j.enganabound.2019.10.017.

[33] A. W. Alshaer, B. D. Rogers, and L. Li, "Smoothed particle hydrodynamics (sph) modelling of transient heat transfer in pulsed laser ablation of al and associated free-surface problems," *Computational Materials Science*, vol. 127, pp. 161—179, 2017. https://doi.org/10.1016/j.commatsci.2016.09.004.

[34] L. Ding, Q. Zheng, Z. Tong, and A. Yu, "Smoothed particle hydrodynamics simulation of transient heat transfer within rotary kiln," *Advanced Powder Technology*, vol. 35, no. 104543, 2024. `https://doi.org/10.1016/j.apt.2024.104543`.

[35] J. H. Jeong, M. S. Jhon, J. S. Halow, and J. v. Osdol, "Smoothed particle hydrodynamics: Applications to heat conduction," *Computer Physics Communications*, vol. 153, no. 1, pp. 71–84, 2003. `https://doi.org/10.1016/S0010-4655(03)00155-3`.

[36] A. Azad, A. A. A. Arani, A. Arefmanesh, and R. Shamsoddini, "Analysis of nanofluid flow and heat transfer inside a channel with smoothed particle hydrodynamics," *International Journal of Thermofluids*, vol. 25, no. 100995, 2025. `https://doi.org/10.1016/j.ijft.2024.100995`.

[37] R. Cherepanov, O. Ivanova, and S. Zelepugin, "Sph simulation of shock-induced chemical reactions in reactive powder mixtures," *Materials Today Communications*, vol. 38, no. 108261, 2024. `https://doi.org/10.1016/j.mtcomm.2024.108261`.

[38] R. Shamsoddini, B. Abolpour, H. Abbaslou, and H. Yarahmadi, "Sph modeling and investigation of the effect of the carbon dioxide entry form on its absorption rate in a microchannel containing absorbent aqueous solution," *Fuel*, vol. 371, no. 132073, 2024. `https://doi.org/10.1016/j.fuel.2024.132073`.

[39] Y. Lin, C. Lüthi, M. Afrasiabi, and M. Bambach, "Enhanced heat source modeling in particle-based laser manufacturing simulations with ray tracing," *Int. J. of Heat and Mass Transfer*, vol. 214, no. 124378, 2023. `https://doi.org/10.1016/j.ijheatmasstransfer.2023.124378`.

[40] L. Yangyang, S. Zhongguo, X. Guang, and L. Ling, "Numerical models for heat conduction and natural convection with symmetry boundary condition based on particle method," *Int. J. of Heat and Mass Transfer*, vol. 88, pp. 433–444, 2015. `https://doi.org/10.1016/j.ijheatmasstransfer.2015.04.105`.

[41] Z. Song, Y. Xing, Q. Hou, and W. Lu, "Second-order symmetric smoothed particle hydrodynamics method for transient heat conduction problems with initial discontinuity," *Processes*, vol. 6, no. 11, 2018. `https://doi.org/10.3390/pr6110215`.

[42] H. P. Hsu, T. W. Tu, and J. R. Chang, "An analytic solution for 2d heat conduction problems with general dirichlet boundary conditions," *Axioms*, vol. 12(5), no. 416, 2023. `https://doi.org/10.3390/axioms12050416`.

[43] N. Subani, F. Jamaluddin, M. A. H. Mohamed, and A. D. H. Badrolhisam, "Analytical solution of homogeneous onedimensional heat equation with neumann boundary conditions," *Journal of Physics: Conference Series*, vol. 1551, no. 012002, 2020. `https://doi.org/10.1088/1742-6596/1551/1/012002`.

[44] L. D. G. Sigalotti, J. Klapp, O. Rendón, C. A. Vargas, and F. Peña-Polo, "On the kernel and particle consistency in smoothed particle hydrodynamics," *Applied Numerical Mathematics*, vol. 108, pp. 242–255, 2016. `https://doi.org/10.1016/j.apnum.2016.05.007`.

[45] W. Dehnen and H. Aly, "Improving convergence in smoothed particle hydrodynamics simulations without pairing instability," *Monthly Notices of the Royal Astronomical Society*, vol. 425, no. 2, pp. 1068—1082, 2012. `https://doi.org/10.1111/j.1365-2966.2012.21439.x`.

[46] C. Hirsch, *Numerical Computation of Internal and External Flows, Volume 1: Fundamentals of Numerical Discretization*. John Wiley & Sons, 1988.

[47] J. D. Anderson, *Computational Fluid Dynamics: The Basics with Applications*. McGraw-Hill, 1997.

[48] C. O. Akeremale, O. A. Olaiju, and Y. S. Hoe, "Finite element method for heat transfer phenomenon on a closed rectangular plate," *EUREKA: Physics and Engineering*, vol. 5, pp. 91–100, 2020. `https://doi.org/10.21303/2461-4262.2020.001422`.